nature communications

Article

https://doi.org/10.1038/s41467-025-64595-5

Membrane-free electrochemical production of acid and base solutions capable of processing ultramafic rocks

Received: 29 June 2025

Accepted: 19 September 2025

Published online: 05 November 2025

Check for updates

Benjamin P. Charnay[1,3], Yuxuan Chen[1,3], Jason W. Misleh[1,3], J. Gage Wright[1,3], Rishi G. Agarwal[1], Ethan R. Sauvé[2], Wei Lun Toh[2], Yogesh Surendranath[2] ✉ & Matthew W. Kanan[1] ✉

Electrochemical production of acid and base from water enables their use as regenerable reagents in closed-loop processes, with attractive applications including CO_2 capture or mineralization and low-temperature production of $Ca(OH)_2$. Conventional systems utilize ion exchange membranes (IEMs) to inhibit H^+/OH^- recombination, which leads to high resistive losses that compromise energy efficiency and poor tolerance for polyvalent metal ions that complicates applications involving mineral resources. Here we use ion transport modeling to guide the design of a system that uses a simple porous separator instead of IEMs. Using H_2 redox reactions for H^+/OH^- production, we demonstrate acid-base production at useful concentrations in the presence of polyvalent impurities with lower energy demand and higher current density than reported IEM-based systems. Cells can be stacked by combining H_2 electrodes into a bipolar gas diffusion electrode, which recirculates H_2 with near-unity efficiency. We show that the cell outputs extract alkalinity from olivine and serpentine as $Mg(OH)_2$ and $Mg_3Si_2O_6(OH)_2$, which remove CO_2 from ambient air to form Mg carbonates. These studies establish the principles for membrane-free electrochemical acid-base production, enabling closed-loop resource recovery and material processing powered by renewable electricity.

Chemical transformations that are critical for carbon management can be driven by sequential application of acid and base. For example, CO_2 can be concentrated from dilute sources by capturing it as (bi)carbonate with base and releasing it with acid[1]. $CaCO_3$ can be converted to slaked lime ($Ca(OH)_2$) at ambient temperature by sequential protonation to form soluble Ca^{2+} and basic precipitation[2]. Similarly, the extraction and purification of metal ions from natural resources or waste products can be achieved by sequential acid leaching and basic precipitation. Extracting $Mg(OH)_2$ from ultramafic rocks by acid-base processing could be used to remove CO_2 from the atmosphere and permanently store it as Mg carbonates[3,4]. Carrying out these pH-swing transformations at scale without stoichiometric waste requires efficient and sustainable methods to generate acid and base from water.

Renewable electricity can be used to drive the dissociation of water into H^+ and OH^-, either at electrodes that carry out acid and base-generating electrocatalytic half-reactions or at the junction of cation and anion exchange membrane components of a bipolar membrane (BPM)[5]. A major source of efficiency loss is deleterious recombination of H^+ and OH^- before they are removed from the cell by flowing electrolyte or utilized in productive chemistry. Recombination is a particularly pernicious problem because the diffusion coefficients of H^+ and

[1]Department of Chemistry, Stanford University; 337 Campus Drive, Stanford, CA, USA. [2]Department of Chemistry, Massachusetts Institute of Technology; 77 Massachusetts Ave, Cambridge, MA, USA. [3]These authors contributed equally: Benjamin P. Charnay, Yuxuan Chen, Jason W. Misleh, J. Gage Wright. ✉e-mail: yogi@mit.edu; mkanan@stanford.edu

OH^- greatly exceed that of all other cations and anions in water due to rapid Grotthuss hopping[6]. Traditionally, this problem is mitigated by incorporating one or more ion-exchange membranes (IEMs) between the acid and base compartments (Fig.1A). Cation-exchange membranes (CEMs) serve to inhibit OH^- transport, whereas anion exchange membranes (AEMs) serve to inhibit H^+ transport. The commercial technology for acid-base co-generation, bipolar membrane electrodialysis (BPMED), combines both modes of inhibition by utilizing a stack consisting of a CEM, AEM, and BPM (Fig.1B). BPMED has been employed for many years in specialty chemical processes[5,7]. More recently, proof-of-concept studies have described the use of IEM-based acid-base co-generation for CO_2 capture from gas streams[8–10] and seawater[11], the conversion of limestone ($CaCO_3$) and H_2O into $Ca(OH)_2$ and CO_2[12,13], and the conversion of gypsum ($CaSO_4$) and H_2O into $Ca(OH)_2$ and H_2SO_4[14,15].

Notwithstanding these precedents, the reliance on IEMs presents a substantial impediment to large-scale application of acid-base co-generation in carbon management and sustainable resource utilization[16]. The narrow ion channels of an IEM restrict ionic current flow, thereby introducing substantial resistive losses even at modest current densities. Furthermore, CEMs become much more resistive in the presence of polyvalent cations (e.g., Ca^{2+}, Mg^{2+}, transition metal ions, etc.) and can be irreversibly damaged by the precipitation of polyvalent hydroxides or carbonates in their channels[17]. Consequently, the NaCl solutions used in CEM-based chloro-alkali technologies must be scrubbed of polyvalent ions to low parts per billion levels to prolong membrane lifetimes[18]. Since most potential applications of acid-base co-generation involve resources with high polyvalent cation content (e.g., $CaCO_3$, $CaSO_4$, ultramafic rocks, seawater), the use of CEMs would require extensive pre-scrubbing. AEMs tolerate polyvalent cations, but most AEMs do not block H^+ transport very well and/or are incompatible with alkaline electrolytes[19]. An advanced H^+ blocking AEM could address this problem but would incur even larger resistive losses[20].

We hypothesized that efficient acid-base co-generation could be achieved without IEMs by using the supporting electrolyte to out-compete H^+ and OH^- transport and mask H^+ as a low-p*K*a anion in a diaphragm flow cell (Fig.1C). This approach enables the use of a simple porous diaphragm to separate the acid and base streams, which greatly reduces the ionic resistance and removes the polyvalent intolerance imposed by IEMs. Additionally, we anticipate negligible energy efficiency (EE) loss from concentration-polarization effects due to a large surplus of supporting ions and free diffusion of all ionic species. Herein, we develop a transport model that predicts the effect of competitive electrolyte migration on the efficiency of electrochemical acid-base co-generation. Guided by this model, we design a simple 2-compartment cell that generates acid and base solutions at useful concentrations (up to 1.275 M) with efficiencies exceeding the state-of-the-art membrane electrodialysis systems and that tolerates polyvalent cation impurities. Optimal performance is achieved by using mixed electrolytes in which Cl^- is employed to outcompete OH^- transport and SO_4^{2-} binds H^+ as HSO_4^-. To minimize the cell potential, we utilize the H_2 oxidation reaction (HOR) and H_2 evolution reaction (HER) for H^+ and OH^- generation, respectively[12,21–23]. By combining HOR and HER gas diffusion electrodes (GDEs) into a bipolar gas diffusion electrode (BPGDE), we show that cells can be combined into a stack such that H_2 produced by HER is consumed by HOR with near-unity efficiency (Fig.1D).

To demonstrate the utility of the acid and base solutions generated by the cell, we use them to perform closed-loop processes that extract $Mg(OH)_2$ and $Mg_3Si_2O_6(OH)_2$ from olivine and serpentine, respectively. In sharp contrast to the inertness of olivine and serpentine, these materials carbonate rapidly under 1 atm CO_2 in an aqueous suspension to form $Mg(HCO_3)_2$. We also show that the $Mg(OH)_2$ extracted from olivine carbonates under wet conditions in ambient air within 8 months to form nesquehonite ($MgCO_3{\cdot}3H_2O$). The approach demonstrated here enables the use of electrochemical acid-base generation to drive key chemical transformations in carbon management and sustainable resource utilization.

Results and discussion

Acid-base generating cell design, modeling, and performance

To evaluate our strategy for acid-base generation, we fabricated a cell consisting of two flowing electrolyte compartments separated by a porous diaphragm (Zirfon) and two GDEs (Fig. 2A and Fig. S1). Each

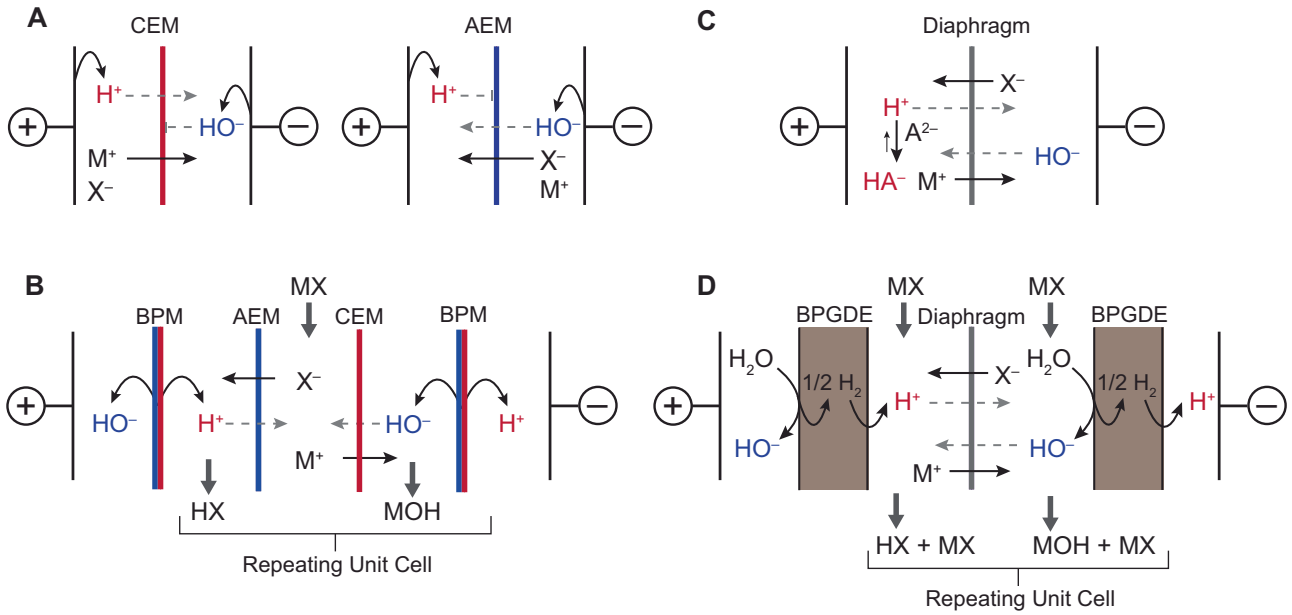

Fig. 1 | Comparison of approaches to generating acid and base solutions. **A** Conventional acid-base generating schemes that use either a CEM to inhibit OH^- crossover (left) or an AEM to inhibit H^+ crossover (right). **B** Schematic of a BPMED system, which uses a BPM to dissociate H_2O into H^+ and OH^- and a combination of a CEM and AEM to generate separate acid and base streams. **C** Acid-base generation using a diaphragm separator instead of IEMs. Suppressing recombination relies on out-competing H^+ and OH^- transport with excess electrolyte ions and "masking" H^+ as a low-pKa anion. **D** Design for a IEM-free stack using a BPGDE to generate H^+ and OH^- by HOR and HER, respectively.

https://doi.org/10.1038/s41467-025-64595-5

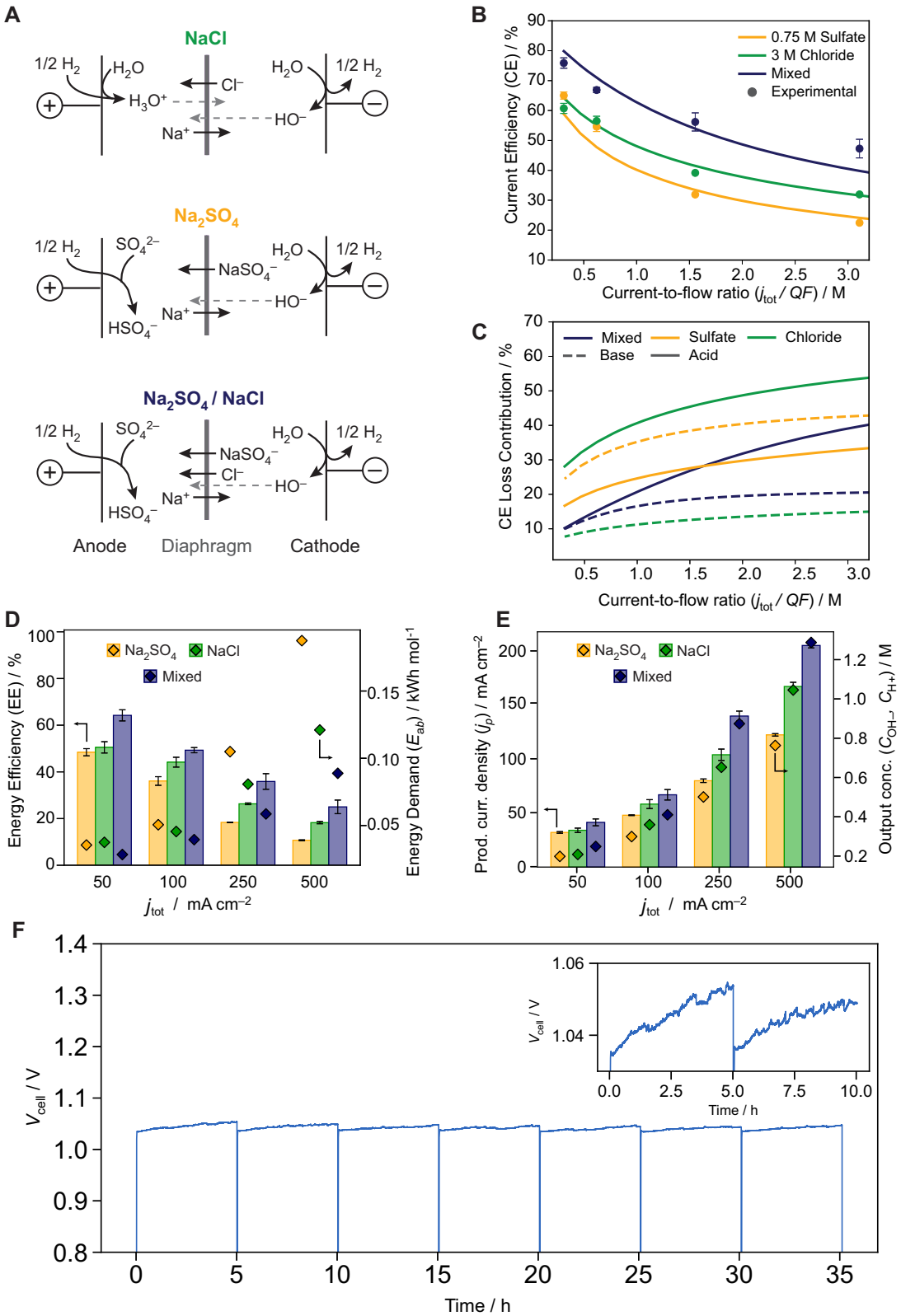

Fig. 2 | Design and performance of membrane-free acid-base-producing electrochemical cell. A Ion transport schemes for three electrolytes. **B** Model and validation of CE at different current-to-flow ratios, which correspond to what the output concentrations would be if CE were 100%. The actual output concentrations are obtained by multiplying the value of the current-to-flow ratio on the x-axis by the corresponding CE value (Table S2). Error bars were calculated from the standard error of the data ($n = 3$). Error bars are rendered for all points, where not visible they are smaller than the marker. **C** Contributions of H^+ and OH^- to the loss of CE as a function of the current-to-flow ratio. Note that 100% − sum of contributions = predicted CE. **D** E_{ab} and EE values for a range of j_{tot} at a constant Q = 0.1 mL min^{-1}. Error bars were calculated from the standard error of the data ($n = 3$). **E** Corresponding values for productive current density and output acid and base concentrations. Error bars were calculated from the standard error of the data ($n = 3$). **F** Cell voltage vs. time trace for a 35 h run at $j_{tot} = 100$ mA cm^{-2} and Q = 0.1 mL min^{-1} cm^{-2} in mixed NaCl/ Na_2SO_4 electrolyte containing Mg and Si impurities. The cell was operated in reverse polarity for 60 s every 5 h. The average V_{cell} is 1.04 V. V_{cell} decays by 1-2 mV h^{-1} (inset), but it is recovered by brief reverse polarization. Voltage data is not *iR* corrected.

electrolyte compartment was assembled out of a 3D printed plate and gaskets for sealing such that the thickness of the flowing anolyte and catholyte layers is only 810 μm each, which reduces solution resistance. A GDE with a Pt/C catalyst layer was used for the anode and one with a PtNi/C catalyst layer was used for the cathode because of their superior performance for HOR and HER, respectively, and their use in large-scale industrial processes[24]. While Pt is a precious metal, at the modest loadings used in GDEs it is not a barrier to scaling. A cost sensitivity analysis of Proton Exchange Membrane electrolyzers showed that reduction of Pt loading by an order of magnitude represented less than a 5% reduction in the overall cost basis of the device[25]. The use of GDEs facilitates H_2 transport to the anode catalyst and clears H_2 efficiently at the cathode to prevent bubble formation.

Acid-base generation with this cell is performed by flowing electrolyte through the two compartments at a fixed volumetric rate per electrode area (Q) while applying a fixed total current density (j_{tot}) and supplying the anode with H_2. To simplify the operation of the cell for our initial experiments, H_2 was supplied to the anode from an external source rather than using the cathodic H_2. The ability to recirculate the H_2 produced by the cathode for consumption at the anode at high efficiency was demonstrated for a stack configuration (see below).

The key performance metrics for electrochemical acid-base co-generation are the current density for productive acid and base generation (j_p), the energy demand per mol of acid and base generated (E_{ab}), the concentration of the acid and base outputs (C_{H+} and C_{OH-}), and the stability of the system over time and to the impurities in the input salt solution. j_p is given by Eq. 1:

$$j_p = j_{tot} \cdot CE \tag{1}$$

where CE is the current efficiency, which is the percentage of the current that results in productive acid and base generation. 100% CE corresponds to zero recombination of H^+ and OH^-. E_{ab} is determined by Eq. 2:

$$E_{ab} = \frac{V_{cell} \cdot F}{CE} \tag{2}$$

where V_{cell} is the measured steady-state cell voltage and F is Faraday's constant. V_{cell} includes the thermodynamic voltage and resistive losses (iR) as well as the HOR and HER overpotentials. V_{cell} and CE can also be used to calculate the EE according to Eq. 3:

$$EE = \frac{0.0592 \cdot \Delta pH \cdot CE}{V_{cell}} \tag{3}$$

where $0.0592 * \Delta pH$ is the thermodynamic minimum cell voltage for a given pH difference between the output acidic and basic solutions. Finally, C_{H+} and C_{OH-} are determined by Eq. 4:

$$C_{H^+} = \frac{j_p}{Q \cdot F} \tag{4}$$

where Q is the volumetric flow rate through the cell compartment. Note that $C_{H+} = C_{OH-}$ if the anolyte and catholyte flow rates are the same.

Since acid-base generation with this design relies on out-competing H^+ and OH^- transport with other ions, the composition of the electrolyte is critical to maximizing CE. We focused on electrolytes made from NaCl and Na_2SO_4 because these salts are the most abundant and lowest-cost choices. With a pure NaCl electrolyte, acid is generated exclusively as H_3O^+ (Fig. 2A). While H_3O^+ is the strongest possible acid in H_2O, the very high mobility of H^+ is expected to negatively impact CE. With SO_4^{2-}- containing electrolytes, electrogenerated H^+ can be masked as HSO_4^-, which is a weaker acid than H_3O^+ (pKa 2 vs. pKa 0) but still strong enough to leach cations from ultramafic rocks (see below). Since HSO_4^- must oppose the electric field to cross the separator and has a relatively low diffusion coefficient, the use of SO_4^{2-} is expected to improve CE[26]. This masking effect has been leveraged in the context of BPMED[27] but is expected to play a stronger role in the diaphragm flow cell because H^+ would already be blocked to some extent by the presence of an AEM.

To guide optimization of the electrolyte composition and gain insight into the physicochemical phenomena that affect cell performance, we developed a model that predicts the steady state concentration of all the ions in the catholyte and anolyte streams for a given electrolyte composition and j_{tot}/Q ratio. The model functions by employing a damped fixed-point iteration algorithm to simultaneously solve the coupled equations that describe ion transport, acid-base and ion-pairing equilibria, and the deviations from ideality captured by the activity coefficients (γ) (see Model Design). Since j_{tot}/Q determines the concentration of H^+ and OH^- generated by the electrodes and the model calculates the transport of all the ions, the model directly predicts the steady-state acid and base concentrations (C_{H+} and C_{OH-}), which can be used to calculate the predicted j_p and CE by Eqs. 4 and 1. Note that C_{H+} includes both the H_3O^+ and HSO_4^- concentrations.

Acid-base generation with our cell was first evaluated by performing a series of short (15-90 min) runs at variable j_{tot} (50–500 mA cm^{-2}) using fixed Q (0.1 mL min^{-1} cm^{-2} for both anolyte and catholyte) with three different electrolytes: 3 M NaCl, 0.75 M Na_2SO_4, and 3 M NaCl + 0.75 M Na_2SO_4. For each experiment, the steady-state V_{cell} was measured and C_{OH-} and C_{H+} (which are necessarily equal) were determined by potentiometric titration of the output catholyte and anolyte with HCl and NaOH standards, respectively. The C_{OH-} was used to calculate CE and j_p and then CE and V_{cell} were used to calculate E_{ab} and EE according to Eqs. 2 and 3, respectively.

Figure 2B shows the predicted and experimental values for CE as j_{tot} was varied. The x-axis is the ratio j_{tot}/QF, which has units of concentration corresponding to the output acid and base concentrations that would be attained if CE were 100%. The predicted curves showed good quantitative agreement with the data for both the pure NaCl and mixed NaCl + Na_2SO_4 electrolytes, and only a slight offset for the pure Na_2SO_4 electrolyte. The CE increases in the order Na_2SO_4 < NaCl <mixed NaCl + Na_2SO_4 electrolyte, with an unexpectedly large benefit afforded by the mixed electrolyte.

The model provides insight to explain the electrolyte-dependence of CE by revealing the current contributions of each ion (Fig. S2). Figure 2C shows the contributions of H^+ and OH^- crossover to the loss in CE as a function of j_{tot}/QF. (H^+ crossover includes both H_3O^+ and HSO_4^- for the Na_2SO_4 -containing electrolytes). With the NaCl electrolyte, H_3O^+ crossover is the major source of CE degradation, accounting for ~27% CE loss at 50 mA cm^{-2} and rising to 60% at 500 mA cm^{-2}, while OH^- crossover accounts for only 5 and 11%, respectively. Upon switching to pure Na_2SO_4, H_3O^+ transport is attenuated by the formation of HSO_4^-. The ability of this electrolyte to mitigate H^+ crossover is limited, however, because a substantial portion of the SO_4^{2-} ions are masked as $NaSO_4^-$ ion pairs (Fig. S2) and there is also a small amount of diffusive crossover of HSO_4^-. Because of the lower mobility and lower concentration of $NaSO_4^-$ [28] compared to Cl^-, there is substantially greater OH^- crossover from the catholyte in Na_2SO_4 vs. the NaCl electrolyte, which more than offsets the difference in H^+ crossover and thereby leads to lower CE.

In the case of the mixed electrolyte, OH^- crossover is mitigated by the supporting Cl^- as compared to the pure Na_2SO_4 electrolyte. More strikingly, the H^+ crossover is reduced compared to both the NaCl and Na_2SO_4 electrolytes, much more than would be expected from simply having a higher Na^+ concentration in the anolyte (except at the highest j_{tot}, where it is the same for the mixed and Na_2SO_4 electrolytes). The model reveals that this outsized benefit arises because γ > 1 for H_3O^+ and γ < 1 for all other species in this highly non-ideal electrolyte. As a

result, HSO_4^- formation increases and $NaSO_4^-$ decreases, which reduces H^+ crossover and improves CE.

Key performance metrics of the acid-base generating cell across the three electrolytes are summarized in Fig. 2D, which shows the E_{ab} and EE values, and Fig. 2E, which shows the j_p and the output C_{H+} and C_{OH-} values over the j_{tot} range of 50–500 mA cm^{-2}. Complete electrolyte speciation data is shown for 3 M NaCl in Fig. S5 and V_{cell} values are provided in table S2. The mixed electrolyte showed the best performance, generating acid and base at concentrations ranging from 0.26 to 1.25 M with the corresponding E_{ab} of 0.03 to 0.116 kWh mol^{-1} and j_p of 42 to 206 mA cm^{-2}. The E_{ab} values correspond to V_{cell} values of 0.90 to 1.54 V and EE values of 64 to 19%. Although EE is highest for the mixed electrolyte, the V_{cell} values are lower for the NaCl electrolyte, which may arise from the lower viscosity and the higher free H_3O^+ concentration in the anolyte, both of which raise the conductivity of the NaCl electrolyte.

To assess stability, the two-compartment cell was operated in longer runs using mixed NaCl + Na_2SO_4 electrolyte that had been used to process ultramafic rocks (see below). This recycled electrolyte was found to contain ~300 μM each of Mg and Si impurities by ICP-OES (table S4). At j_{tot} = 100 mA cm^{-2} and Q = 0.1 mL min^{-1} cm^{-2}, V_{cell} exhibited a steady increase of ~1 mV h^{-1}. We hypothesized that this voltage decay is the result of scale deposits on the cathode from precipitation of $Mg(OH)_2$ or SiO_2 as base is generated. One method that is used to reverse voltage decay from small-scale deposits in industrial saline concentrating stacks is to periodically apply a brief reverse polarization to generate acid that dissolves the deposits[29]. We therefore used a duty cycle where the cell was operated in reverse polarity at the same j_{tot} for 60 s every 5 h. The net current passed is 99.7% of that which would have been passed over the same time span without the reverse polarization duty cycle. As seen in Fig. 2F, reverse polarization repeatedly restored the voltage decay that occurred over each 5 h period, demonstrating that this strategy is viable for maintaining efficiency in long-term operation of the cell. The average voltage restoration after every step was 6 mV ± 1 mV with individual steps having a decay rate of 1.6 mV h^{-1} ± 0.4 mV h^{-1}. The CE measured by titration after 25 h of operation was 68%, agreeing with the value predicted by the model (71%).

The performance summarized in Fig. 2 demonstrates that our strategy for acid-base production can achieve EE, throughput, and impurity tolerance that rival state-of-the-art IEM-based systems. In the commercial BPMED technology, a stack of cells composed of an AEM, a CEM, and a BPM convert a concentrated salt solution into acid and base solutions along with a depleted salt solution (Fig. 1A)[5,7]. In the best performance reported to date, a BPMED system operated with an E_{ab} ranging from 0.073 to 0.145 kWh mol^{-1} at j_p of only ~30 mA cm^{-2} to generate solutions ranging from 0.6 to 2.1 M[30]. At an E_{ab} of 0.060 kWh mol^{-1}, our cell operates at a j_p of 140 mA cm^{-2} while generating 0.87 M output solutions. While our system generates acid and base solutions with high salt concentration, the salt is not likely to pose a problem for most closed-loop applications, as demonstrated below for ultramafic processing. BPMED also requires water removal when used in a closed loop system because it effectively dilutes the salt solution by generating separate acid and base solutions, which has an additional modest energy demand but substantially increases process complexity. Critically, BPMED systems require rigorous removal of polyvalent cations from the input salt streams to avoid irreversible CEM damage, while our system can tolerate polyvalents with periodic polarity reversals. Recently reported acid-base generating cells for CO_2 capture and slaked lime production have exhibited either substantially higher energy demand and/or even lower j_p than BPMED[2,10,13–15,31]. In addition, some of these systems have shown rapid and irreversible voltage decay arising from incompatibility with polyvalent cations (see table S1).

Practical application of the acid-base generating strategy described above requires a way to combine cells into a stack such that H_2 generated at the cathode of one cell is utilized at the anode of the adjacent cell. We hypothesized that cells could be stacked using a BPGDE, which combines an HER GDE cathode and HOR GDE anode back-to-back so that H_2 can be transported easily from one electrode to the other (Fig. 3A). A previous report demonstrated the use of a BPGDE as a substitute for an IEM whereby H^+ was transported between two acidic compartments by the HER/HOR combination. This prior construct was unable to function without supplying additional current to the cathodic half of the BPGDE, producing excess H_2 to make up for poor hydrogen crossover efficiency from cathode to anode[32]. To be used as a stack element for acid-base generation with our cell design, the BPGDE must generate a large pH gradient, and the H_2 generated at the cathode side must be consumed at the anode side with very high efficiency to avoid large parasitic energy losses associated with supplying makeup H_2. We made a BPGDE by sandwiching a GDE cathode and GDE anode between two bipolar half-plates (Fig. S6). In this experiment, the BPGDE served as the bipolar element for the simple two-cell stack depicted in Fig. 3A. In this design, the BPGDE has access to the H_2 stream supplied to the terminal anode by an internal tee in the electrolyzer hardware to help moderate the pressure in the BPGDE and provide a mechanism to make up for potential H_2 losses. The stack was then operated at j_{tot} = 100 mA cm^{-2} (200 mA total current) and Q = 0.1 mL min^{-1} cm^{-2} using the mixed NaCl + Na_2SO_4 electrolyte.

Figure 3B shows the voltage vs. time traces for the stack and the two component cells over a 25 h segment at j_{tot} = 100 mA cm^{-2} (200 mA total current) and Q = 0.1 mL min^{-1} cm^{-2} using the mixed NaCl + Na_2SO_4 electrolyte. The stack voltage maintained a quasi-steady state value of 2.03 V. The CE was determined by titration at the beginning and end of the 25 h segment to be 73%, which is comparable to the performance of a single cell. The H_2 stream supplying the terminal anode and connected to the BPGDE was supplied 1.025 (± 0.026) equivalents of H_2 relative to what is required to operate a single 1 cm^2 anode at 100 mA cm^{-2}. As the BPGDE produces and consumes exactly 1 equivalent of H_2, it does not in principle require any from the flowing stream except to replace any H_2 losses. In a separate experiment, the BPGDE was not connected to the terminal anode's gas supply and was required to operate only on the H_2 it could produce itself. Under the same conditions of j_{tot} = 100 mA and Q = 0.1 mL min^{-1} cm^{-2} using the mixed NaCl + Na_2SO_4 electrolyte, the BPGDE operated for 24 h with no external gas supply. Throughout this period, the voltage across both cells was below the thermodynamic energy requirement for oxygen evolution and chlorine evolution, indicating both anodes were performing hydrogen oxidation and at least 99.9% of the H_2 generated at the BPGDE's cathode is oxidized at the connected anode (Fig. S7).

Ultramafic rock processing

Olivine (Mg endmember: Mg_2SiO_4) and serpentine (Mg endmember: $Mg_3Si_2O_5(OH)_4$) are attractive resources for CO_2 removal because of their abundance[33–35] and high MgO content. While the reaction of these minerals with CO_2 to form Mg carbonates is thermodynamically favored[36], it is extremely slow under ambient conditions and limited to low conversions because of passivation phenomena[37,38]. Acidic leaching of Mg^{2+} followed by alkaline precipitation provides a way to extract the alkalinity from olivine and serpentine in the form of $Mg(OH)_2$[39], which can react with CO_2 under ambient conditions at useful rates[40,41]. The acid and base solutions generated by our cell were therefore evaluated for their ability to process olivine and serpentine for this purpose (Fig. 4A, B).

To process olivine, the anolyte output from the extended single-cell run described above (Fig. 2F) was combined with five molar equivalents of olivine sand ($Mg_{2-x}Fe_xSiO_4$;, x~0.15, see table S3), where 1 equivalent corresponds to 1 $Mg_{2-x}Fe_xSiO_4$ per 4 H^+ in the anolyte ($HSO_4^- + H_3O^+$). The suspension was stirred until the solution pH rose to >2.5, which took ~48 h, and then separated from the remaining olivine by filtration.

https://doi.org/10.1038/s41467-025-64595-5

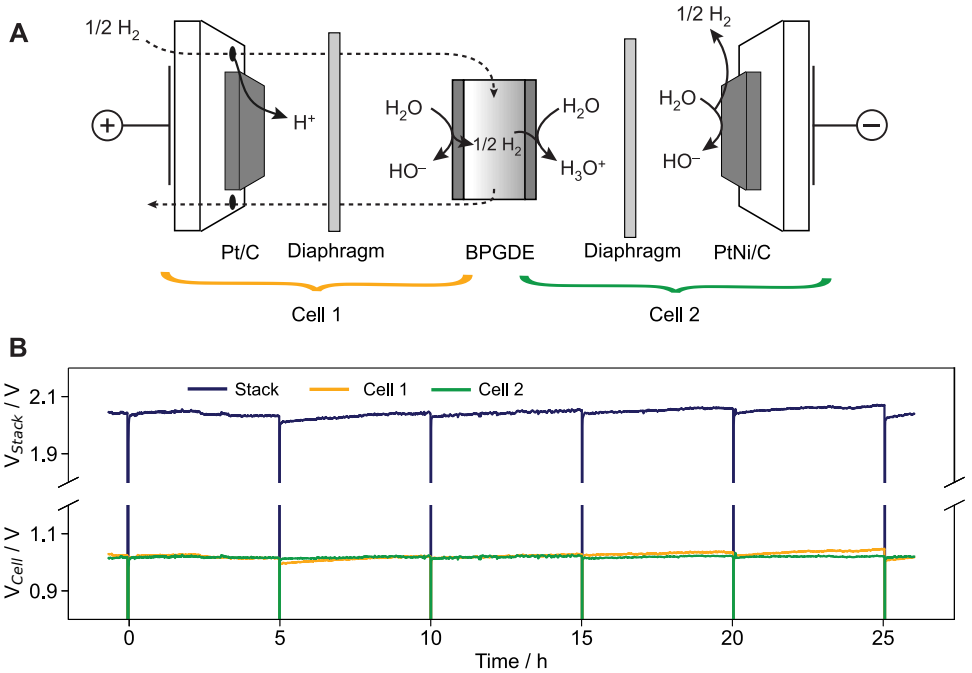

Fig. 3 | Results of the 2-cell stack experiments. A Schematic of a two-cell acid-base generating stack with a BPGDE linking the cells. **B** Voltage vs time trace for a 25 h segment of operating the stack with mixed 3 M NaCl + 0.75 M Na_2SO_4 electrolyte at j_{tot} = 100 mA cm^{-2}, Q = 0.1 mL min^{-1} cm^{-2}. Shown are the full stack voltage and the voltages of the individual cells. Voltage data is not *iR* corrected. The terminal anode was supplied with H_2 at a flow rate corresponding to 1.025 equivalents of H_2 compared to the stoichiometric requirement for the terminal anode. This H_2 supply was connected to the BPGDE by channels in the stack hardware, as shown in (**A**), which allows for the small excess of H_2 supply to the terminal anode to provide H_2 to the BPGDE to compensate for potential H_2 losses.

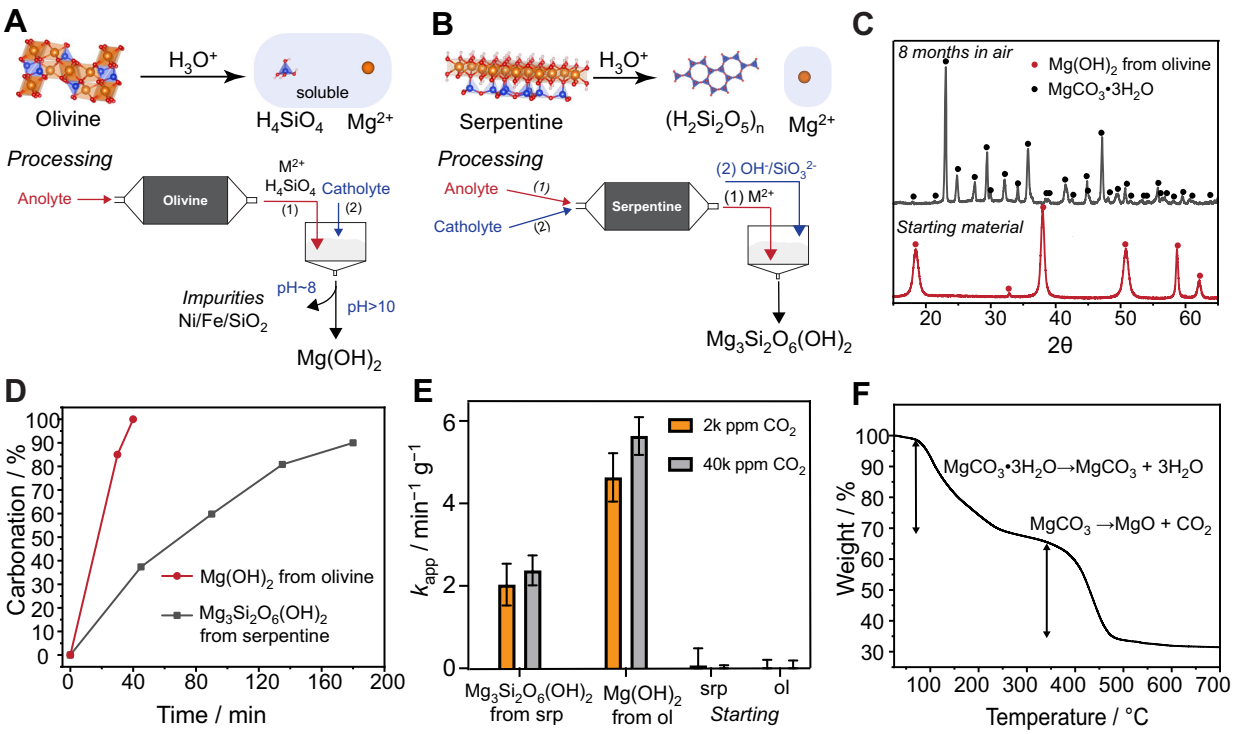

Fig. 4 | Ultramafic processing and CO_2 removal. A Schematics of acid dissolution and processing method for olivine. Orange, blue, red and pink represent Mg, Si, O, and H. **B** Schematics of acid dissolution and processing method for serpentine. **C** pXRD of $Mg(OH)_2$ obtained from olivine processing and its carbonated product after 8 months in air under wet conditions at ambient temperature. **D** Extent of carbonation vs. time under 1 atm CO_2 for $Mg(OH)_2$ obtained from processing olivine and $Mg_3Si_2O_6(OH)_2$ obtained from processing serpentine. **E** Apparent 2nd order rate constants for uptake of CO_2 from dilute streams for $Mg(OH)_2$ obtained from processing olivine (ol) and $Mg_3Si_2O_6(OH)_2$ obtained from processing serpentine (srp). Starting ol and srp showed no measurable uptake. Error bars were calculated from the standard error of the data (n = 2). **F** TGA of magnesium carbonate product from the carbonation of $Mg(OH)_2$ obtained from olivine in air for 8 months.

Since olivine dissolves congruently in acid[42], the contacted anolyte solution at this point contains Mg^{2+}, Fe^{2+}, soluble silicic acid (H_4SiO_4), other metal ion impurities, and the electrolyte components. To remove the Fe, Si, and other impurities[39,43,44], the catholyte was added drop-wise to reach pH~8 and the resulting dark precipitate was separated by filtration. Analysis by SEM-EDX indicated that it is composed predominantly of Si, Fe, and Mg compounds, with a 10:2.3:1.0 Si:Fe:Mg ratio (Fig. S8). The filtrate was then combined with additional catholyte to increase the pH to ~10, which resulted in a white precipitate that was confirmed by powder XRD (pXRD) to be $Mg(OH)_2$ (Fig. 4C). SEM-EDX analysis showed that only trace amounts of Si (< 1 mol%) and no Na, Cl, S or other elements were detected, indicating nearly complete recovery of electrolyte for continued electrolysis (Fig. S9). Based on the amount isolated, the efficiency of converting the acid and base generated by the cell into $Mg(OH)_2$ extracted from olivine is ~90%, with most of the balance accounted for by the extraction of $Fe(OH)_2$.

In addition to this batch experiment, we confirmed that the dissolution of olivine can be performed continuously by flowing an acidic electrolyte through a bed of olivine sand (Fig. S10). By adding olivine as it is dissolved and controlling the flow rate, it is possible to achieve both high proton consumption and essentially quantitative consumption of the olivine with this simple design.

In contrast to olivine, acid digestion of serpentine, a phyllosilicate, only releases the cations and trace amounts of Si species, leaving behind an insoluble, amorphous silica passivation layer that inhibits further dissolution[45]. Previous reports have used energy-intensive ball milling or grinding methods to remove the passivation layer[46,47]. We found that the silica passivation is removed in alkaline solutions (> 0.1 M NaOH) under ambient conditions to form soluble silicate species (e.g., Na_2SiO_3). We therefore developed a procedure to process serpentine consisting of alternating acid (anolyte) and base (catholyte) treatments. For a batch experiment, anolyte was stirred with five molar equivalents of ground serpentine until the pH rose to ~2.5 and then separated by filtration. SEM/EDX analysis indicated a decrease in the Mg:Si ratio of the serpentine after this step and pXRD analysis showed no crystalline SiO_2 phase, which are consistent with the accumulation of an amorphous SiO_2 passivation layer (Fig. S11). Instead of adding the catholyte directly to the contacted anolyte at this point, the catholyte was added to the serpentine to dissolve the SiO_2 layer as a silicate solution. The anolyte and catholyte were then combined, yielding a white precipitate. SEM/EDX showed relatively large particles (100–400 μm) with Mg and Si as the only major cations detected, and pXRD showed only very broad, low-intensity peaks that could not be definitively assigned (Fig. S12). Thermogravimetric analysis (TGA) showed a sharp mass loss at 300 °C–500 °C, which is characteristic of $Mg(OH)_2$ dehydration.

Based on the ratio of this mass loss to the residual mass, the approximate composition of the precipitated material can be assigned as $Mg_3Si_2O_6(OH)_2$, which is the expected composition assuming that the NaOH in the catholyte quantitatively removes the amorphous silica formed from the acidic Mg^{2+} leaching. (Fig. S13)

The reactivities of solids obtained from acid/base processing were compared to the parent minerals by performing carbonation reactions in which 5 wt% slurries of each solid were stirred under 1 atm CO_2 at ambient temperature. Under these conditions, carbonation produces soluble $Mg(HCO_3)_2$. The extent of carbonation was assessed by periodic analysis of the supernatant (see Materials characterization methods). The $Mg(OH)_2$ obtained from olivine fully carbonated into soluble $Mg(HCO_3)_2$ in 45 min, forming a clear solution. The carbonation of $Mg_3Si_2O_6(OH)_2$ obtained from serpentine demonstrated slower kinetics but still reached >90% carbonation in 4 h (Fig. 4D). By contrast, no carbonation was observed for olivine or serpentine under the same conditions. The complete lack of carbonation reactivity for olivine was also confirmed by IR and TGA analysis (Fig. S14).

To compare reactivity at lower partial pressures, the CO_2 uptake kinetics of the various rock samples were also measured in CO_2 absorption experiments for 30 wt% CDR material slurries with CO_2 concentrations of 2000 and 40,000 ppm (Fig. 4E). The apparent rate constants, k_{app}, provide a quantitative descriptor to compare the carbonation reactivity of alkaline solids. Carbonation rates were found to be roughly first order in CO_2, with second-order apparent rate constants of 5.6 min^{-1} g^{-1} and 2.4 min^{-1} g^{-1} found for olivine-derived $Mg(OH)_2$ and serpentine-derived $Mg_3Si_2O_6(OH)_2$, whereas rates of uptake were negligible for olivine and serpentine themselves. Finally, the carbonation of olivine-derived $Mg(OH)_2$ was also tested in ambient air. The solid was kept under wet conditions by adding 1 g H_2O/g material daily. The progress of the carbonation was tracked by analyzing solid content by pXRD. $Mg(OH)_2$ was converted into nesquehonite ($MgCO_3 \cdot 3\ H_2O$) in 8 months (Fig. 4C, F).

The above results enable a preliminary assessment of the energy demand for performing CDR by combining electrochemical acid-base production with isolation of reactive alkalinity from ultramafic rocks in a cyclic process. Balancing throughput and energy, we assume the performance metrics obtained at j_{tot} = 250 mA cm^{-2} (j_p = 140 mA cm^{-2}), for which E_{ab} is 0.066 kWh mol^{-1} (Fig. 2D). Using olivine as the feedstock and assuming 90% efficiency for the extraction of $Mg(OH)_2$, the estimated total energy demand for acid and base generation is 0.134 kWh per mol $Mg(OH)_2$, which corresponds to 2.30 MWh per ton $Mg(OH)_2$. The energy required for extracting and grinding olivine and pumping solutions through the acid-base generator are very modest additional demands, bringing the total to 2.34 MWh per ton $Mg(OH)_2$. One ton of $Mg(OH)_2$ can remove up to 0.75 ton CO_2 as $MgCO_3$ in terrestrial applications or up to 1.5 ton as $Mg(HCO_3)_2$ in aquatic applications. Thus, the energy demand for CDR is estimated as 3.10 MWh/t_{CO2} if the captured form of CO_2 is $MgCO_3$ and 1.55 MWh/t_{CO2} if it is $Mg(HCO_3)_2$. This range compares favorably to leading direct air capture technologies, for which the estimated energy just for capture is estimated as 1.8–2.7 MWh/t_{CO2} and the CO_2 must then be injected subsurface and monitored for centuries[48,49].

The foregoing studies emphasize the power of electrolyte design in enabling high-efficiency acid-base generation without the need for ion exchange membranes. The studies also evince the viability of using reversible H_2 electrocatalysis to drive acid-base formation with minimal H_2 loss in a stack configuration and the use of the resulting acid-base equivalents to convert olivine and serpentine to active materials for irreversible CO_2 removal. By exploiting electrolyte non-idealities and binding acid or base equivalents, electrochemical acid-base production using the designs described here could be extended to enable an array of resource recovery and mineral transformations powered by renewable electricity.

Methods

Materials

Olivine (100 mesh) was purchased from Teton Supply Co. Serpentine (~ 10 × 10 x 10 cm) was purchased from merchants on Etsy. Sodium chloride (99.9%) was purchased from Sigma Aldrich. Sodium sulfate (99.9%) was purchased from Fisher Scientific. H_2O was taken from a Nanopore filtration system (18.2 MΩ). All chemicals were used without further purification. Porous diaphragm Zirfon PERL 500 UTP was obtained from Agfa. Gas Diffusion Electrodes were obtained from De Nora: 0.5 mg cm^{-2} PtNi/C with no Teflon wetproofing and 0.85 mg cm^{-2} Pt/C with wetproofing.

Procedure for electrochemical acid/base generation

Electrolyte preparation. Electrolyte was prepared by dissolving the relevant salts in deionized water in volumetric flasks. Prepared electrolyte was stored in plastic bottles. The pH of the 3 M NaCl electrolyte was 6.45 ± 0.01, the pH of the 0.75 M Na_2SO_4 electrolyte was

6.45 ± 0.05, and the pH of the 3 M NaCl + 0.75 M Na_2SO_4 mixed electrolyte was 5.76 ± 0.04 as measured by pH meter.

Single cell experiment

The single cell was assembled from machined Grade V Ti blocks that deliver H_2 and electrolyte, plates for flowing electrolyte past the electrodes, and gaskets (Fig. S1). 3D-printed plastic plates with rubber o-rings seal each electrode against a flow field and interface with the liquid ports on the blocks. The alternate side of each plate defines the active electrode area and seals the GDE's edges from electrolyte while sealing against a PTFE gasket to define channels that direct the solution path across the GDE. The solution compartments for the anolyte and catholyte are only 32 thou or 810 μm thick. Each electrolyte compartment is 0.08 cm^3, and the active area of the electrodes is 1 cm^2. Alignment is assured by 4 plastic rods in each corner of the cell. A piece of Zirfon and an accompanying polyurethane gasket separate the anode and cathode assemblies. The final full cell assembly is placed into a Palmgren vise and compressed to 200 in. lbs. Co-generation of acid and base was performed using a BioLogic VSP-3e potentiostat in galvanostatic mode performing the hydrogen oxidation reaction at the anode and the hydrogen evolution reaction at the cathode. Solution was flowed through the cell with a 4 channel, 12 roller Masterflex Ismatec Reglo ICC Digital peristaltic pump.

Two cell stack experiment

The two-cell stack (Fig. S6) has the same design as the single cell with the inclusion of a BPGDE assembly that serves as the anode of one cell and the cathode of the next. Implementation of the internal tee gas flow architecture simply consists of putting extra holes in the flow plates and gaskets such that H_2 supplied to the electrode block is also allowed to flow through these holes past the liquid compartments. The plates for the BPGDE assembly were made conductive via electroless silver plating[50]. Prior to any full-stack measurements, the BPGDE must be pre-charged with H_2 and any atmosphere in the porous transport layer displaced. This is accomplished by running current through only cell 1 and thus generating excess H_2 at the cathode side of the BPGDE. This is done at an applied current density of 100 mA/cm^2 with the bipolar plate acting as a current collector for the cathode/working electrode for between 30 and 60 s. Following pre-charging, the stack is run in reverse for 1 min at 100 mA/cm^2. This is done as a pretreatment/break-in process that improves stack performance. The stack was operated galvanostatically while the stack and cell voltages were measured by two channels of a BioLogic VSP-3e in stack mode.

Current efficiency measurement

Current efficiency was measured by potentiometric titration of catholyte and/or anolyte against an HCl or NaOH standard, respectively. Secondary standards were standardized against dry Na_2CO_3 or potassium hydrogen phthalate, respectively.

$$\frac{\text{Volume}_{\text{standard}} \cdot C_{\text{standard}}}{j_{\text{tot}} \cdot A \cdot t_{\text{collection}}/F} = \text{CE} \quad (5)$$

Ultramafic rock processing and carbonation procedures

Preparation of ground rock. As-purchased serpentine samples were cut into pieces by a diamond saw, crushed by a jaw crusher, ball-milled in a SPEX mixer mill, and sieved to obtain a particle size fraction from 75 to 106 microns. The composition of the ground sample was examined by X-Ray fluorescence and pXRD.

Acid leaching of olivine in a batch reactor

Olivine (5 molar equivalents) was mixed with the anolyte from the cell output. The solution was stirred at 500 rpm under ambient conditions. The solution pH was checked by pH paper. The reaction was stopped with an ending pH ~3, which corresponds to >99% of H^+ (H_3O^+ and HSO_4^-) consumption. For a more quantitative pH measurement, aliquots were taken and diluted 100x by adding deionized water. The pH was read by pH Sensor InLab Routine Pro-ISM.

Acid leaching of olivine in a flow contactor

~25 g of 100 mesh (150 microns) olivine was packed into a glass column (d = 0.5 cm). Anolyte stream was flowed in at a rate controlled by a valve at the bottom of the glass column. The pH of the inlet and outlet stream was recorded to evaluate the efficiency of the contactor. A contact time of ~30 min is needed to achieve >90% proton consumption efficiency for an inlet of 0.1 M acid. The contact time can be shortened to <15 min with the use of finer olivine particles (~75 microns) for an inlet of 0.1 M acid.

Precipitation of impurities and $Mg(OH)_2$ from olivine leaching solution

The anolyte contacted with olivine in the batch reactor was separated from the remaining olivine and the catholyte from the cell output was added dropwise at a rate of 0.3 mL min^{-1}. Addition was continued until the pH reached ~8 (indicated by pH paper), which resulted in a dark precipitate. The precipitate was filtered off and washed with 50 mL starting electrolyte, which was added to the filtrate. Additional catholyte was added at 0.3 mL min^{-1} into the filtrate to produce $Mg(OH)_2$. After all the catholyte was added, the slurry was filtered and the regenerated electrolyte was recovered (pH 10.63 ± 0.01). The product was washed with 20 mL water, resulting in a gel. The gel then was dried under vacuum oven at 50 °C overnight to form a solid, which was crushed, washed with 20 mL water and dried at 120 °C in air overnight before mass measurement and further characterization.

Procedure for processing serpentine

Anolyte from the cell output was stirred with five molar equivalents of serpentine at ambient temperature. The reaction was stopped when the pH of the solution reached 2.5–3 and the slurry was centrifuged to separate the solid. The solid was then stirred with an equal volume of catholyte for 1–2 h to generate a silicate-rich stream from dissolution of the amorphous SiO_2 layer and the solid was filtered off. The derived silicate-rich filtrate was added drop-wise into contacted anolyte filtrate to form a precipitate. The material was isolated by filtration and then dried under vacuum at 50 °C.

Carbonation of $Mg(OH)_2$ or silicate under 1 atm CO_2

CO_2 was bubbled into DI water until the pH reached ~4. 50–100 mg material was suspended in 10 mL CO_2-saturated DI water in a 20 mL vial. The headspace was filled with 1 atm CO_2. The slurry was stirred at 500 rpm at ambient temperature. To analyze the extent of carbonation, the suspension was filtered at each time point to separate the supernatant from remaining solid. The supernatant was fully dried at 50 °C. Any $Mg(HCO_3)_2$ present in the solution is transformed into $MgCO_3$ by this drying step. The solid separated by filtration (i.e., uncarbonated material) was washed with ethanol once and dried under vacuum overnight. The mass of the product isolated from the supernatant and the mass of the unreacted solid were recorded and used to calculate the extent of carbonation.

Carbonation in air under ambient conditions

100 mg of $Mg(OH)_2$ obtained by precipitation from the olivine leaching solution was placed in a 20 mL glass vial without a cap. 100 μL DI water was added to wet the solid daily. Carbonation was tracked by periodically taking pXRD patterns of dried materials. Before analysis, the solid material was dried under vacuum at 30 °C overnight to remove any water.

CO_2 uptake kinetic measurements

The rate of CO_2 uptake in mol dm^{-3} min^{-1} is described by

$$\frac{d[CO_{2(aq)}]}{dx} = k_{app} \cdot [CO_{2(aq)}] \quad (6)$$

Where k_{app} is the apparent rate constant and has units of min^{-1}. To compare the CO_2 uptake kinetics of the parent minerals and derived alkaline solids, we measured k_{app} normalized to sample mass. Breakthrough experiments were performed by passing a mixed gas stream of Ar (40 amu) and CO_2 (44 amu) through a vial containing water sample and sending the output to an in-line mass spectrometer. The ratio of the MS signal for peaks at 44/40 amu was calibrated in the range of 1000–40,000 ppm CO_2 by sparging known concentrations through a background vial containing 1 mL of water. For all sample measurements, the mixed gas stream of Ar and CO_2 was first sparged into a vial containing 1 mL of water to obtain a background trace. Once the signal had stabilized, data was collected for 10 min. The 'background' vial was then replaced with a vial containing 0.5 g of sample with 1 mL of water and when the signal had stabilized, data was collected for 10 min. The calibration curve was used to convert the ratio of the MS signal for peaks at 44/40 amu to the concentration of gaseous CO_2 in ppm. Henry's Law was used to calculate the concentration of aqueous CO_2, assuming gaseous CO_2 in the headspace and dissolved CO_2 in solution are at equilibrium.

Estimation of energy demand for CDR

The energy demand for CDR was estimated for a case in which the acid and base outputs of the cell are used to extract $Mg(OH)_2$ from olivine and the $Mg(OH)_2$ is carbonated under ambient conditions. Two acid-base equivalents are consumed per mol $Mg(OH)_2$. Using $E_{ab} = 0.060$ kWh mol^{-1} (corresponding to $j_p = 240$ mA cm^{-2}) and an efficiency of converting acid and base into $Mg(OH)_2$ of 0.9, the energy demand of the echem system (E_{echem}) for generating $Mg(OH)_2$ can be estimated as $2^*E_{ab}/0.9 = 0.134$ kWh $mol_{Mg(OH)2}^{-1} = 2.30$ MWh $t_{Mg(OH)2}^{-1}$. The energy demand for extracting and grinding olivine to moderate particle sizes (~100 μm) is estimated to be 20 kWh $t_{olivine}^{-1}$ [51], which corresponds to 25.6 kWh $t_{Mg(OH)2}^{-1}$ assuming 32.5 wt% Mg in the olivine (Table S4). To estimate the pumping energy demands, we assume that the echem system will operate with a total flow rate of 120 L m^{-2} h^{-1} (0.1 mL cm^{-2} min^{-1} for each of catholyte and anolyte) and that the pumping energy is 0.2 kWh m^{-3} [11]. Assuming output concentrations of 0.87 M for the acid and base, the total volume of liquid that must be pumped through the echem system is 87.5 m^3 $t_{Mg(OH)2}^{-1}$, which corresponds to an energy demand of 17.5 kWh $t_{Mg(OH)2}^{-1}$.

Materials characterization methods

Characterization of the materials produced in the course of processing ultramafic rocks was performed in part using methods described previously[52].

Scanning electron microscopy (SEM) and energy dispersive X-ray (EDX) spectroscopic imaging were performed on a Thermo-Fisher Scientific Apreo S LoVac SEM equipped with an Everhart-Thornley Detector (ETD). Element compositions were analyzed using an XFlash 6 − 60 SDD EDS detector. Powder samples were affixed to the SEM holder via a double-sided, adhesive-coated, conductive carbon sheet obtained from Ted Pella. The sample was coated with 15 nm carbon or gold.

Powder X-ray diffraction (pXRD) measurements were done on a PANalytical Empyrean using copper (8.04 keV) as the source. The instrument was operated at 45 kV, 40 mA. Data were collected over a 2θ range of 15° – 65° or 10° – 65° with a step size of 0.025° – 0.05°. Phase identification was performed using Highscore.

TGA was carried out on SDT 650 high-temperature DSC/TGA. Samples of ~5 mg were sealed in alumina crucibles purchased from TA Instruments. Measurements were performed under 50 mL min^{-1} dry N_2 flow with a temperature ramp rate of 20 °C min^{-1}.

Inductively coupled plasma optical emission spectroscopy (ICP-OES) was performed on a Thermo Scientific iCAP 6300 Duo View Spectrometer. The uncertainty in the values in table S4 represents the propagated uncertainty from the linear regression parameters.

Model Design

In our acid-base generating cell, the anodic reaction generates H^+ and the cathodic reaction generates OH^-, creating an imbalance of charge and concentration that drives the movement of ions in solution. To compute the steady state concentrations (SSC) of ions in the cell, it is necessary to solve the steady state equations that define, on the timescale of a given packet of electrolyte's presence in the current path, how much of every ionic species is introduced, transported, and neutralized. In the literature this has been accomplished by the simultaneous solution of partial differential equations in a finite element analysis simulation package such as COMSOL Multiphysics[7,53]. However, given the complexity of the coupled partial differential equations that govern ion transfer in our system, we developed an alternative approach that greatly reduces the computational resources required.

The mass transfer of an ion, j is described by the Nernst-Planck Equation:

$$J_j = -D_j \nabla c_j - \frac{D_j z_j F}{RT} c_j \nabla \phi + c_j v \quad (7)$$

where J_j is the flux, and the three terms on the right correspond to the contributions from diffusion, migration and advection, respectively[54]. Assuming no advection and considering mass transfer in only one spatial dimension (along the path of current), the current carried by an ion j is given by:

$$i_j = -FAz_j J_j = FAz_j D_j \frac{\partial c_j}{\partial x} + \frac{F^2 A}{RT} z_j^2 D_j c_j \frac{\partial \phi}{\partial x} \quad (8)$$

where the first term on the right-hand side is the diffusion current and the second term is the migration current. The total current, i_{tot}, is then the sum of the partial currents from each ion in solution:

$$i_{tot} = FA \sum_k z_k D_k \frac{\partial c_k}{\partial x} + \frac{F^2 A}{RT} \cdot \frac{\partial \phi}{\partial x} \sum_k z_k^2 D_k c_k \quad (9)$$

This equation is difficult to utilize because it requires knowledge of the electric field (ϕ) experienced by each ion. However, with the assumption of a linear electric field, the fraction of the total migration current carried by an ion j can be expressed as the transference number of j, t_j:

$$t_j = \frac{|z_j| \lambda_j c_j}{\sum_k |z_k| \lambda_k c_k} \quad (10)$$

where λ_j is the specific molar conductivity of ion j. Combining Eqs. 9 and 10, replacing partial derivatives with finite differences, and rearranging for partial current yields:

$$i_j = \left(i_{tot} - FA \sum_k z_k D_k \frac{\Delta c_k}{\Delta x} \right) \cdot \frac{|z_j| \lambda_j c_j}{\sum_k |z_k| \lambda_k c_k} + FAz_j D_j \frac{\Delta c_j}{\Delta x} \quad (11)$$

In this equation, A and Δx are modulated by the MacMullin number to account for the tortuosity and porosity of the separator (i.e., Zirfon)[55]. It is important to note that Eq. 5 assumes ideal behavior;

approaches to describing the behavior of real electrolytes will be discussed below.

The finite timescale that controls the proceedings of the electrochemical reactions and resulting mass transfer can be thought of as the residence time of a packet of electrolyte in the electroactive compartment of the cell. Conveniently, the actual value of the residence time need not be calculated, as it is reflected in the ratio of current to flow rate. This value is equivalent to the expected concentration of acid or base at the output of the reactor under 100% current efficiency conditions. That being the case, we can recast Eq. 11 in terms of deviation from this 100% scenario to express the steady-state concentration of ion j, c_j^{ss} as:

$$c_j^{ss} = c_j^{\circ} - \frac{i_j^{ss}}{rF} \tag{12}$$

where c° is the concentration in the case of 100% current efficiency and r is the flow rate of electrolyte. For the supporting electrolyte ions, c° is equal to the input concentration.

We can now see in Eq. 12 that the SSC for a given ion is dependent on the SSC of all other ions in the reactor. This demands the solution of a minimum of two coupled equations in the trivial case of no supporting electrolyte. In this case, the steady state concentrations of OH^- and H^+ are each 0, as all the current must be carried by one or the other, resulting in complete neutralization of both. This case also demonstrates the inextricable link between the concentrations of H^+ and OH^-, as the transport of one in one direction is equivalent to the transport of the other in the opposite direction. Adding a supporting electrolyte of any kind adds a minimum of 4 additional equations to be solved, an anolyte and catholyte instance of the anion and cation of the salt. In the event that some of those ions can participate in chemical equilibrium, i.e. SO_4^{2-} with H^+, then that equilibrium must also be satisfied in accordance with a local equilibrium approximation (LEA) and may also be liable to deviations from ideality[56].

To solve these many simultaneous equations, a damped fixed-point iteration method was employed. Mathematically, a fixed point of a function is an input that returns an identical value as the output, and in reaction modeling refers to a steady state[57]. The solutions were found using a simple Python program where Eq. 13c is performed until $\Delta\mathbf{C}^{ss}$ is below some cutoff, chosen to be 1 pM for this work as this cutoff uniformly resulted in convergence.

$$\mathbf{C} = [c_1, c_2, c_3 \cdots c_m] \tag{13a}$$

$$\mathbf{C}_{n=0}^{ss} = \mathbf{C}^{\circ} \tag{13b}$$

$$\mathbf{C}_{n+1}^{ss} = \omega\left(\mathbf{C}^{\circ} - \frac{\hat{\mathbf{I}}(\mathbf{C}_n^{ss})}{rF}\right) + (1-\omega)\mathbf{C}_n^{ss} \tag{13c}$$

In this context, the capitalized "**C**" represents the collection of all ionic concentrations, and $\hat{\mathbf{I}}(\mathbf{C})$ denotes the execution of Eq. 11 on all species. The term ω serves as a damping term, modulating the pace of the computation to prevent errors and facilitate convergence. In this instance, ω was set to 33% which is known to enhance convergence rate and reliability[58]. Due to the inherent properties of transport, where an increase in the quantity of a species leads to an increase in its transport, this iteration will always converge to a unique set of fixed points. These fixed points define the efficiency of the electrolysis cell and can be viewed as self-solving[59]. Approaches to addressing non-idealities were implemented to improve model accuracy. Concentrations were converted to activities using activity coefficients calculated by the Pitzer equation, which are included in the PyEquIon package. Aqueous speciation and coupled equilibria are also activity-corrected and handled by the PyEquIon package. Diffusion coefficients were divided by the relative viscosity of the electrolyte solution in line with Stokesian behavior: (below)[60,61].

$$D_j = \frac{D_j^{\circ}}{\eta_{rel}} \tag{14}$$

where η_{rel} is the relative dynamic viscosity of the solution compared to the reference solvent and D_j° is the diffusion coefficient in the reference solvent. The framework of this model is generalizable to any finite-gap steady-state device with non-selective separators but could be adapted to situations with selective membranes.

Qualitative Description of Ion-Transport Model

The fixed-point iteration model was implemented in a simple Python program and can run a single set of conditions in ~5 seconds on an M1 ProMacbook Pro. All speciation and activity coefficients in a given round of the convergence loop were calculated by the PyEquIon package. For each round, diffusion for all ions was calculated first, ignoring the resulting charge imbalance. Then, starting from the initial charge imbalance of electrogenerated species ± charge imbalance from diffusion, ionic current is calculated for each ion based on its transference number. This process would necessarily result in a fully charge-balanced system after every iteration, but this is purposefully prevented by the ω damping term to avoid oscillation. The transient charge imbalance during the convergence loop is incompatible with PyEquIon, so fictitious $Cl^-$and Na^+ concentrations are used in early steps for balance; the final result of a given convergence never includes this fictitious balancing term. We note that the PyEquIon package has since been deprecated and replaced with a PyEquIon2.

Reporting summary

Further information on research design is available in the Nature Portfolio Reporting Summary linked to this article.

Data availability

Source data are provided with this paper.

Code availability

Code used to perform ion transport modeling is provided in the linked repository.

References

1. Cao, T. N.-D. et al. Unraveling the potential of electrochemical pH-swing processes for carbon dioxide capture and utilization. *Ind. Eng. Chem. Res.* **62**, 20979–20995 (2023).
2. Ellis, L. D., Badel, A. F., Chiang, M. L., Park, R. J.-Y. & Chiang, Y.-M. Toward electrochemical synthesis of cement—An electrolyzer-based process for decarbonating CaCO3 while producing useful gas streams. *Proc. Natl. Acad. Sci. USA* **117**, 12584–12591 (2020).
3. *A Research Strategy for Ocean-Based Carbon Dioxide Removal and Sequestration*. (National Academies Press, 2022). https://doi.org/10.17226/26278.
4. Rau, G. H. et al. Direct electrolytic dissolution of silicate minerals for air CO2 mitigation and carbon-negative H2 production. *Proc. Natl Acad. Sci.* **110**, 10095–10100 (2013).
5. Pärnamäe, R. et al. Bipolar membranes: a review on principles, latest developments, and applications. *J. Membr. Sci.* **617**, 118538 (2021).
6. Agmon, N. The Grotthuss mechanism. *Chem. Phys. Lett.* **244**, 456–462 (1995).
7. Mareev, S. A. et al. A comprehensive mathematical model of water splitting in bipolar membranes: impact of the spatial distribution of fixed charges and catalyst at bipolar junction. *J. Membr. Sci.* **603**, 118010 (2020).
8. Jin, S., Wu, M., Jing, Y., Gordon, R. G. & Aziz, M. J. Low energy carbon capture via electrochemically induced pH swing with electrochemical rebalancing. *Nat. Commun.* **13**, 2140 (2022).

9. Ali, F., Modak, S. & Kwabi, D. G. Assessing the performance limits of electrochemical CO2 separation using exergy loss analysis and zero-dimensional modeling. *ACS Sustain. Chem. Eng.* **11**, 16995–17005 (2023).
10. Zhu, P. et al. Continuous carbon capture in an electrochemical solid-electrolyte reactor. *Nature* **618**, 959–966 (2023).
11. Digdaya, I. A. et al. A direct coupled electrochemical system for capture and conversion of CO2 from oceanwater. *Nat. Commun.* **11**, 4412 (2020).
12. Mowbray, B. A. W., Zhang, Z. B., Parkyn, C. T. E. & Berlinguette, C. P. Electrochemical cement clinker precursor production at low voltages. *ACS Energy Lett.* **8**, 1772–1778 (2023).
13. Zhang, Z. et al. Porous metal electrodes enable efficient electrolysis of carbon capture solutions. *Energy Env. Sci.* **15**, 705–713 (2022).
14. Lammers, L. N. et al. Electrolytic sulfuric acid production with carbon mineralization for permanent carbon dioxide removal. *ACS Sustain. Chem. Eng.* **11**, 4800–4812 (2023).
15. Miao, R. K. et al. Electrified cement production via anion-mediated electrochemical calcium extraction. *ACS Energy Lett.* **8**, 4694–4701 (2023).
16. Lucas, É et al. Asymmetric bipolar membrane for high current density electrodialysis operation with exceptional stability. *ACS Energy Lett.* **9**, 5596–5605 (2024).
17. Mikhaylin, S. & Bazinet, L. Fouling on ion-exchange membranes: classification, characterization and strategies of prevention and control. *Adv. Colloid Interface Sci.* **229**, 34–56 (2016).
18. European Commission. Joint Research Centre. Institute for Prospective Technological Studies. *Best Available Techniques (BAT) Reference Document for the Production of Chlor-Alkali: Industrial Emissions Directive 2010/75/EU (Integrated Pollution Prevention and Control)*. (Publications Office, 014).
19. Yu, S. et al. Proton blockage PVDF-co-HFP-based anion exchange membrane for sulfuric acid recovery in electrodialysis. *J. Membr. Sci.* **653**, 120510 (2022).
20. Jaroszek, H., Mikołajczak, W., Nowak, M. & Pisarska, B. Comparison of the applicability of selected anion-exchange membranes for production of sulfuric acid by electro-electrodialysis. *DESALINATION WATER Treat.* **64**, 223–227 (2017).
21. Holze, S., Jörissen, J., Fischer, C. & Kalvelage, H. Hydrogen consuming anodes for energy saving in sodium sulphate electrolysis. *Chem. Eng. Technol.* **17**, 382–389 (1994).
22. Gilliam, R. J. et al. Low voltage electrochemical process for direct carbon dioxide sequestration. *J. Electrochem. Soc.* **159**, B627 (2012).
23. Yan, L., Bao, J., Shao, Y. & Wang, W. An electrochemical hydrogen-looping system for low-cost CO2 capture from seawater. *ACS Energy Lett.* **7**, 1947–1952 (2022).
24. DeMarinis, M., Castro, E. S. D., Allen, R. J. & Shaikh, K. Structures and Methods of Manufacture for Gas Diffusion Electrodes and Electrode Components. US6103077A (2000).
25. Mayyas, A., Ruth, M., Pivovar, B., Bender, G. & Wipke, K. *Manufacturing Cost Analysis for Proton Exchange Membrane Water Electrolyzers*. NREL/TP-–6A20-72740, 1557965 https://www.osti.gov/servlets/purl/1557965/, https://doi.org/10.2172/1557965 (2019).
26. Weil, K. G. V. M. M. Lobo: Physical Sciences Data 41. Handbook of Electrolyte Solutions, Part A,. V. M. M. Lobo, J. L. Quaresma: Physical Sciences Data 41. Handbook of Electrolyte Solutions, Part B, ISBN Vol. 41: 0-444-98847-5, Elsevier Amsterdam, Oxford, New York, Tokyo 1989, 2354 Seiten, Preis: Dfl. 1.400, –. *Berichte Bunsenges. Für Phys. Chem.* **95**, 1305–1305 (1991).
27. Mutahi, G., van Lier, J. B. & Spanjers, H. Leveraging organic acids in bipolar membrane electrodialysis (BPMED) can enhance ammonia recovery from scrubber effluents. *Water Res* **265**, 122296 (2024).
28. Hnedkovsky, L., Wood, R. H. & Balashov, V. N. Electrical conductances of aqueous na\textlesssub\textgreater2SO4, H2SO4, and Their Mixtures: Limiting Equivalent Ion Conductances, Dissociation Constants, and Speciation to 673 K and 28 MPa. *J. Phys. Chem. B* **109**, 9034–9046 (2005).
29. Tanaka, Y. Chapter 2 Electrodialysis Reversal. in *Membrane Science and Technology* (ed. Tanaka, Y) vol. 12 383–404 (Elsevier, 2007).
30. Reig, M., Casas, S., Valderrama, C., Gibert, O. & Cortina, J. L. Integration of monopolar and bipolar electrodialysis for valorization of seawater reverse osmosis desalination brines: Production of strong acid and base. *Desalination* **398**, 87–97 (2016).
31. Willauer, H. D., DiMascio, F., Hardy, D. R. & Williams, F. W. Feasibility of CO2 extraction from seawater and simultaneous hydrogen gas generation using a novel and robust electrolytic cation exchange module based on continuous electrodeionization technology. *Ind. Eng. Chem. Res.* **53**, 12192–12200 (2014).
32. Furuya, N., Kawamura, M. & Mineo, N. Hydrogen-ion exchange using a bipolar gas-diffusion electrode. *Denki Kagaku* **56**, 666–667 (1988).
33. de Coninck, H. & Benson, S. M. Carbon dioxide capture and storage: issues and prospects. *Annu. Rev. Environ. Resour.* **39**, 243–270 (2014).
34. Pronost, J. et al. Carbon sequestration kinetic and storage capacity of ultramafic mining waste. *Environ. Sci. Technol.* **45**, 9413–9420 (2011).
35. Bide, T. P., Styles, M. T. & Naden, J. An assessment of global resources of rocks as suitable raw materials for carbon capture and storage by mineralisation. *Trans. Inst. Min. Metall. Sect. B Appl. Earth Sci.* **123**, 179–195 (2014).
36. Oconnor, W. Aqueous mineral carbonation: mineral availability, pretreatment, reaction parametrics, and process studies. https://doi.org/10.13140/RG.2.2.23658.31684.
37. Vink, J., Giesen, D. & Ahlrichs, E. *Olivine Weathering in Field Trials; Effect of Natural Environmental Conditions on Mineral Dissolution and the Potential Toxicity of Nickel*. (2023).
38. Béarat, H. et al. Carbon sequestration via aqueous olivine mineral carbonation: role of passivating layer formation. *Environ. Sci. Technol.* **40**, 4802–4808 (2006).
39. Scott, A. et al. Transformation of abundant magnesium silicate minerals for enhanced CO2 sequestration. *Commun. Earth Environ.* **2**, (2021).
40. Rausis, K., Stubbs, A. R., Power, I. M. & Paulo, C. Rates of atmospheric CO2 capture using magnesium oxide powder. *Int. J. Greenh. Gas. Control* **119**, 103701 (2022).
41. Harrison, A. L., Power, I. M. & Dipple, G. M. Accelerated carbonation of brucite in mine tailings for carbon sequestration. *Environ. Sci. Technol.* **47**, 126–134 (2013).
42. Oelkers, E. H., Declercq, J., Saldi, G. D., Gislason, S. R. & Schott, J. Olivine dissolution rates: a critical review. *Chem. Geol.* **500**, 1–19 (2018).
43. Clark, R. W. & Bonicamp, J. M. The Ksp-solubility conundrum. *J. Chem. Educ.* **75**, 1182 (1998).
44. Choppin, G. R., Pathak, P. & Thakur, P. Polymerization and Complexation Behavior of Silicic Acid: A Review. *Main Group Met. Chem.* **31**, 53–72 (2008).
45. Feng, B., Lu, Y., Feng, Q., Ding, P. & Luo, N. Mechanisms of surface charge development of serpentine mineral. *Trans. Nonferrous Met. Soc. China* **23**, 1123–1128 (2013).
46. Rim, G. *Coupled Kinetic and Mechanistic Study of Carbonation of Silicate Materials with Tailored Transport Behaviors for CO2 Utilization* (Columbia University, United States — New York, 2020).
47. Rim, G., Wang, D., Rayson, M., Brent, G. & Park, A. H. A. Investigation on abrasion versus fragmentation of the si-rich passivation layer for

enhanced carbon mineralization via CO2 partial pressure swing. *Ind. Eng. Chem. Res.* **59**, 6517–6531 (2020).
48. Keith, D. W., Holmes, G., St Angelo, D. & Heidel, K. A process for capturing CO2 from the atmosphere. *Joule* **2**, 1573–1594 (2018).
49. Deutz, S. & Bardow, A. Life-cycle assessment of an industrial direct air capture process based on temperature–vacuum swing adsorption. *Nat. Energy* **6**, 203–213 (2021).
50. Wright, J. G., Charnay, B. P., Rabinowitz, J. A., Mariano, R. G. & Kanan, M. W. Rapid prototyping of lab-scale electrolysis cells using stereolithography and electroless plating. *Device* **1**, 100049 (2023).
51. Chapter 3 - Size Reduction and Energy Requirement. in *Mineral Processing Design and Operations (Second Edition)* (eds. Gupta, A. & Yan, D.) 71–121 (Elsevier, Amsterdam, 2016). https://doi.org/10.1016/B978-0-444-63589-1.00003-4.
52. Chen, Y. & Kanan, M. W. Thermal Ca2 + /Mg2+ exchange reactions to synthesize CO2 removal materials. *Nature* **638**, 972–979 (2025).
53. Ortega, A. et al. Modelling water dissociation, acid-base neutralization and ion transport in bipolar membranes for acid-base flow batteries. *J. Membr. Sci.* **641**, 119899 (2022).
54. Bard, A. J., Faulkner, L. R. & White, H. S. *Electrochemical Methods: Fundamentals and Applications*. (Wiley & Sons, 2022).
55. de Groot, M. T. & Vreman, A. W. Ohmic resistance in zero gap alkaline electrolysis with a Zirfon diaphragm. *Electrochim. Acta* **369**, 137684 (2021).
56. Samson, E., Marchand, J. & Beaudoin, J. J. Modeling the influence of chemical reactions on the mechanisms of ionic transport in porous materials: An overview. *Cem. Concr. Res.* **30**, 1895–1902 (2000).
57. Kafri, H. Q., Khuri, S. A. & Sayfy, A. A fixed-point iteration approach for solving a BVP arising in chemical reactor theory. *Chem. Eng. Commun.* **204**, 198–204 (2017).
58. Evans, C., Pollock, S., Rebholz, L. G. & Xiao, M. A Proof That Anderson acceleration improves the convergence rate in linearly converging fixed-point methods (But Not in Those Converging Quadratically). *SIAM J. Numer. Anal.* **58**, 788–810 (2020).
59. Ciesielski, K. On Stefan Banach and some of his results. *Banach J. Math. Anal.* **1**, 1–10 (2007).
60. Korosi, A. lexander & Fabuss, B. M. Viscosities of binary aqueous solutions of sodium chloride, potassium chloride, sodium sulfate, and magnesium sulfate at concentrations and temperatures of interest in desalination processes. *J. Chem. Eng. Data* **13**, 548–552 (1968).
61. Marcellos, C. F. C. et al. PyEquIon: a Python Package For Automatic Speciation Calculations of Aqueous Electrolyte Solutions. (PyEquIon, 2021).

Acknowledgements

This work was supported by the Solar Photochemistry and Catalysis Programs of the Chemical Sciences, Geosciences, and Biosciences Division, Office of Basic Energy Sciences, US Department of Energy, DE-SC0021633, the Accelerated Decarbonization Program of the Canadian Institute for Advanced Research, and MAC3 and the Stanford Woods Institute for the Environment Big Ideas for the Oceans. Part of this work was performed at the Stanford Nano Shared Facilities (SNSF), supported by the National Science Foundation under award ECCS-2026822. J.G.W. is supported by a Stanford Graduate Fellowship and B.P.C. is supported by a Chevron Fellowship in Energy. E.R.S. is supported by an NSERC Postdoctoral Fellowship. J.W.M. is supported by an NSF GRFP fellowship.

Author contributions

Conceptualization: BPC, YC, RGA, WLT, YS, MWK, Methodology: BPC, YC, RGA, JWM, JGW, ERS, Investigation: BPC, YC, RGA, JWM, JGW, ERS, Formal Analysis: BPC, JGW, JWM, YC, RGA, Software: BPC, JGW, RGA, Visualization: BPC, YC, JGW, ERS, YS, MWK, Funding acquisition: MWK, YS, Project administration: MWK, YS, Supervision: MWK, YS, Writing – original draft: BPC, YC, RGA, YS, JWM, JGW, MWK, Writing – review & editing: BPC, YC, JGW, JWM, RGA, WLT, YS, MWK.

Competing interests

Two PCT patent applications have been filed based on this work. The authors are inventors on one or both applications.

Additional information

Supplementary information The online version contains supplementary material available at https://doi.org/10.1038/s41467-025-64595-5.

Correspondence and requests for materials should be addressed to Yogesh Surendranath or Matthew W. Kanan.

Peer review information *Nature Communications* the anonymous reviewers for their contribution to the peer review of this work. A peer review file is available.